

The divergent fates of primitive hydrospheric water on Earth and Mars

Jon Wade^{1*}, Brendan Dyck^{2,6}, Richard M. Palin³, James D.P. Moore⁴, Andrew J. Smye⁵

¹ Department of Earth Sciences, University of Oxford, South Parks Road, Oxford OX1 3AN, UK

² Department of Earth Sciences, University of Cambridge, Cambridge, CB2 3EQ, UK

³ Department of Geology and Geological Engineering, Colorado School of Mines, Golden, CO 80401, USA

⁴ Earth Observatory of Singapore, Nanyang Technological University, Singapore

⁵ Department of Geosciences, Pennsylvania State, PA 16801, USA

⁶ Department of Earth Sciences, Simon Fraser University, Burnaby, BC, V5A 1S6, Canada

* corresponding author: jon.wade@earth.ox.ac.uk

Despite active transport mechanisms into the Earth's mantle, water has been present on our planet's surface for most of geological time^{1,2}, yet water disappeared from the Martian surface soon after its formation. While the Martian water inventory was partially depleted by loss to space via photolysis following the collapse of the planet's magnetic field³⁻⁵, widespread serpentinisation of Martian crust^{6,7} attests to metamorphic hydration reactions having played a critical role in its sequestration. Here we quantify the relative volumes of water that could be removed from each planet's surface via the burial and metamorphism of hydrated mafic crusts, and calculate mineral transition-induced bulk-density changes at elevated pressure-temperature conditions in each. The metamorphic mineral assemblages in relatively FeO-rich Martian lavas can hold ~25% more structurally-bound H₂O than those in metamorphosed terrestrial basalts, and transport it to greater relative depths

within the Martian interior. Our calculations suggest that in excess of 9 vol. % of the Martian mantle may contain hydrous mineral species as a consequence of surface reactions, compared to ~4 vol. % of the Earth. Furthermore, neither primitive nor evolved hydrated Martian crust show significantly different bulk densities compared to their anhydrous equivalents, in contrast to mafic terrestrial crust that transforms to eclogite upon dehydration. This would have allowed efficient over-plating and burial of early Martian crust in a stagnant lid tectonic regime, thus providing a significant sink for hydrospheric water and a mechanism to oxidise the Martian mantle. Conversely, relatively buoyant mafic crust and hotter geothermal gradients on Earth reduced the potential for upper mantle hydration early in its geological history, leading to water being retained close to its surface, thus creating conditions conducive for the evolution of complex multicellular life.

Surface water has existed on Earth for the vast majority of geologic time¹, with its volume having remained approximately constant since the end of the Archean (2.5 Ga) and initiation of subduction-driven plate tectonics². However, despite evidence for it having once possessed liquid water, the modern-day surface of Mars is essentially dry and lacks any widespread features of active plate tectonics⁸. The loss of surficial water from Mars since its formation has been attributed to both photolysis in the upper atmosphere and/or sequestration into the crust via metamorphic hydration reactions⁹. Although loss to space by atmospheric sputtering and hydrodynamic escape likely became increasingly viable after cessation of the Martian magnetic field at c. 4.1 Ga³⁻⁵, uncertainties in its efficiency, the timing of field collapse, and the initial water inventory suggest that this process alone may not have depleted the entire volume of the hydrosphere over the lifetime of the planet¹⁰⁻¹². Instead, petrological evidence for crustal hydration—a notably more efficient mechanism to sequester large amounts of H₂O from a planet’s hydrosphere—is present as serpentinized surface basalts^{6,7} and the widespread distribution of oxidised hydrated phyllosilicate minerals⁷. The disassociation of water during such

silicate-mineral hydration reactions and the subsequent loss of hydrogen to space, for example, may account for the presence of oxidised magnetite¹³ and maghemite in Martian meteorite NWA7034 and the Gusev crater rocks it resembles¹⁴, while the source region of Martian SNC meteorites is much more reduced^{14,15}.

Aside from the proportion of iron, the terrestrial and Martian mantles have broadly similar chondritic major element compositions^{16,17}. The abundance of iron in planetary mantles—and hence erupted surface material—is primarily controlled by the prevailing oxygen fugacity (fO_2) of planetary accretion, which was higher during Martian core formation than terrestrial core formation. As a result, terrestrial basalts are relatively FeO-poor (~7–10 wt. %)¹⁸ compared to more FeO-rich (~17 wt. %)¹⁹ basalts derived from the Martian upper mantle. As bulk-rock composition is the primary control on the mineral assemblages that stabilise during surface hydration and metamorphism at elevated pressure (P) and temperature (T) conditions, these compositional differences likely played a critical role in controlling each planet’s bulk geochemistry and surface water budget over geological time. Here, we have quantified the balance between mantle hydration and density in both terrestrial and Martian interiors using integrated thermal and petrological modelling. We show that metamorphosed primitive and evolved Martian basalts can hold ~25% more structurally-bound water in hydrous minerals than terrestrial equivalents can, with the majority stable to greater depths within Mars (>90 km) than within Earth (~70 km). In addition, time-integrated mass-balance calculations show that the absolute volume of the Martian mantle that has potentially been hydrated over geological time (>9%) is at least twice as large as the terrestrial mantle (~4%).

Although achieved at different times in their cooling histories, in order to model their surface evolutions we considered a mantle potential temperature (T_P) of 1650 °C for both the terrestrial and Martian primitive basalts, and a lower bound of 1400 °C for evolved rocks. SNC meteorites

indicate that the rate of secular cooling on Mars was conservatively about three-times faster than that of Earth²⁰. We combined this with a plate cooling model, taking into account secular cooling and radiogenic heat production in order to calculate likely aerotherms and geotherms through the lithospheres of each planet. The petrological changes that would occur in the end member cases of primitive and evolved, fully hydrated and fluid-undersaturated crust during each planet's geological evolution were then investigated using thermodynamic phase equilibrium modelling at conditions defined by these P – T gradients. For Mars, we utilised bulk compositions for primitive (Fastball) and evolved (Backstay) basalts, and for Earth we utilised a high-MgO Archean tholeiitic basalt and a modern-day MORB (see *Methods*). We considered metamorphism at pressures of 8–26 kbar (Earth) and 3–10 kbar (Mars), and temperatures of 500–1200 °C. Hydration at lower-grade conditions is controlled by phases belonging to the serpentine, phyllosilicate, and clay mineral groups, with higher water contents. Phase diagrams for each rock type considering fluid-saturated conditions are presented in *Extended data* Figures 1–4.

Calculated water contents and bulk-rock densities for each terrestrial and Martian protolith as a function of depth within the planetary interior are shown in Figure 1. Unlike terrestrial modern MORB, the higher water-carrying potential of high-MgO Archean terrestrial basalts is primarily a result of their more refractory nature, with the absence of quartz allowing water-bearing amphiboles to persist to higher temperatures²¹, and thus greater depths in the mantle (Figure 1a). A similar trend characterises Martian materials, with metamorphosed primitive basalt (Fastball) being comprised mostly of hornblendic amphibole at subsolidus P – T conditions. Evolved Martian melts (Backstay-type compositions) contain a smaller proportion of water-bearing minerals at these temperatures, but retain their water to greater depths. In both cases, the net water-bearing potential of Martian materials exceed those of their terrestrial counterparts.

The decomposition of amphibole during prograde metamorphism marks the terminus of hydrous mineral stability in both terrestrial and Martian materials. Indeed, evolved Martian basalts may retain amphibole to temperatures in excess of 1200 °C, where they are calculated to become Ti-rich, matching observed compositions from Martian meteorites²². Although hydration extends to similar absolute depths on both bodies, the shallower Martian aerotherm implies that the volume fraction of silicate Mars that may be hydrated following crustal subduction is about double that of the Earth (Figure 2). Additionally, the faster cooling of Mars²⁰ progressively extends the depth of hydration, exacerbated by the presence of more evolved basalts over-plating the Martian surface and the negative Clapeyron slope for hornblende dehydration. The effect that hydration has on bulk-rock density heightens this effect; metamorphosed terrestrial basalts are all significantly less dense—and hence buoyant—when fluid-saturated, and undergo densification upon dehydration (Figure 1b). The relatively Fe-rich Martian materials are, however, calculated to exhibit relatively little volume expansion during hydration, with more evolved basalts showing minimal change in bulk-rock density, and significant densification (>5%) of a water-bearing restite, post-melting. Here, the main reaction products of high-pressure hornblende dehydration at the fayalite–magnetite–quartz (FMQ) buffer are clinopyroxene, plagioclase, garnet, magnetite, and silicate melt.

Hydrated Martian basalts generate relatively high degrees of melt (~30%) at moderate temperatures (~800–900 °C), leaving a hydrous residual assemblage of neutral or negative buoyancy. This suggests that, unlike on Earth, hydrated materials could have been transferred into its mantle via sagduction or crustal delamination^{23,24} (Figure 3). Mars may therefore have undergone extensive hydration of its mantle simply by magmatic overplating, burial and metamorphism of hydrated surface basalts. This mechanism may also have been responsible for delivering oxidised material to the source region of the Martian surface basalts¹⁴. On Earth, the increased buoyancy of hydrated Archaean greenstones and steeper geotherm limit the water-

carrying capacity of over-plated material. The secular evolution of plate tectonics and the transition from early-Earth high-MgO basalts to modern-day MORB basalts (with an inherently lower water-carrying capacity)²⁵ further limits the mechanisms of water transport into the terrestrial interior. Mars shows the opposite trend, as its secular cooling, high water-carrying capacity of surface basalts, and the neutral buoyancy of hydrated materials acted to preferentially sequester water back into its interior.

On Earth, surface water is transported into the upper mantle primarily by K-amphibole²⁶, which typically forms in hydrated MgO-rich metabasalt. In contrast, more ferruginous Martian basalts stabilize iron-rich hydrous phases at equivalent P – T conditions, such as hornblende and biotite (Extended Data - Figure 5). The decomposition of hornblende during metamorphism is controlled by P , T , and fO_2 , with lower temperatures and reducing conditions specifically favouring its stability²⁷. Owing to its smaller size, Martian aerotherms have higher dT/dP gradients than geotherms on Earth, which suggests that hydrous phases, such as amphibole, comprise a greater proportion of its mantle. Rock-hydration reactions may therefore be important both as a surface water-loss mechanism and as a means to transport oxidised material to upper-mantle depths. However, as hydration reactions are typically associated with a decrease in bulk-rock density, re-entrainment of crustal material into the mantle—either via burial or subduction—may be limited until dehydration has occurred.

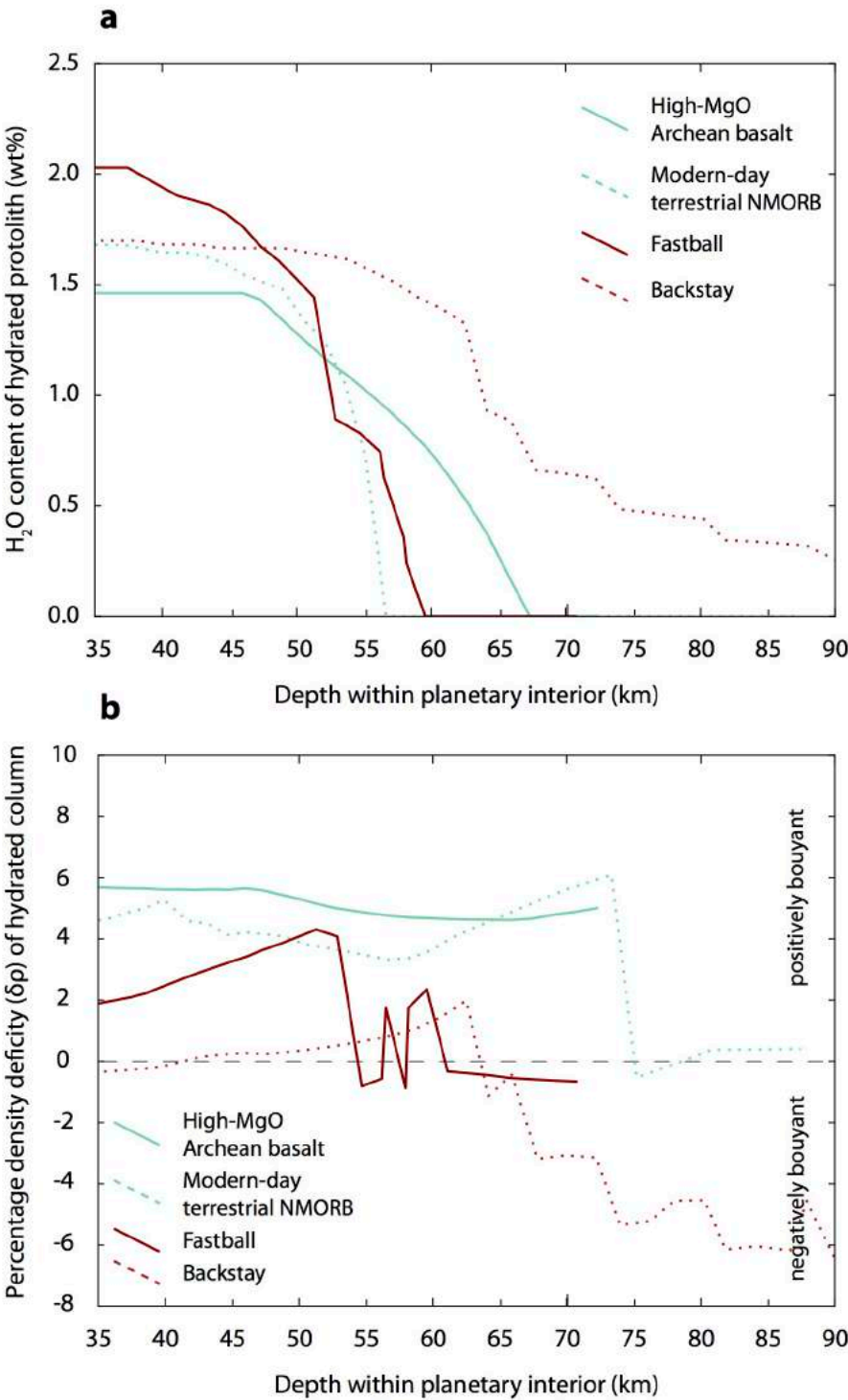
In the absence of subduction-driven plate tectonics early in each planet’s geologic history²⁸, both Earth and Mars would have experienced significant basaltic surface over-plating. Elevated mantle potential temperatures would have led to higher degrees of partial melting and more voluminous, low-viscosity magmas. Erupted²⁹ or emplaced³⁰ in the presence of water, they may be assumed to efficiently hydrate³¹. Our results show that the ability of a planet to retain surface water is not simply a function of its bulk composition or size, but also its accretion history, not least the

oxygen fugacities prevailing during core formation. By setting the bulk silicate FeO content, mantle redox state places a first-order control on the amount of amphibole production and stability, and hence high-pressure water-carrying minerals. Earth-like planetary size allows a long-lived steep geotherm, which in turn promotes dewatering of hydrated phases close to the planetary surface, and thus the efficient return of buried water to the surface (Figure 1). In contrast, Mars exhibits evidence of long-lived water reservoirs both extant as sub-surface ice³² and as hydrated crust³³. These, together with the elevated FeO contents of the Martian mantle and smaller planetary size, results in significant water sequestration into the Martian mantle via increased amphibole content and the production of hydrous restite of neutral or negative buoyancy. Taken concurrently, the individual water-carrying capacities of erupted magmas and their respective fates upon burial are key to understanding the early hydrological cycles on each planet.

Acknowledgments: JW acknowledges receipt of an NERC Independent Research Fellowship NE/K009540/1. J.D.P.M was supported by the National Research Foundation (NRF) of Singapore under the NRF Fellowship scheme (National Research Fellow award NRF-NRFF2013-04) and by the Earth Observatory of Singapore, the NRF, and the Singapore Ministry of Education under the Research Centres of Excellence initiative.

Author Contribution: J.W. conceived the idea in discussion with A.J.S. and performed initial calculations. R.M.P. and B.D. performed the petrological modelling. Thermal modelling was performed by J.D.P.M. All authors contributed to writing the final manuscript.

The authors declare no competing financial interests.



182
183 **Figure 1 | Calculated petrophysical properties for each modelled basaltic protolith. a**, Plot of
184 the structurally-bound water content (wt. %) in metamorphosed primitive and evolved basalt on
185 Earth and Mars. **b**, Relative density deficit between a crustal column comprised of fully hydrated
186 and nominally anhydrous metabasalt ($\delta\rho = (\rho_{\text{anhydrous}} - \rho_{\text{hydrated}})/\rho_{\text{anhydrous}}$).

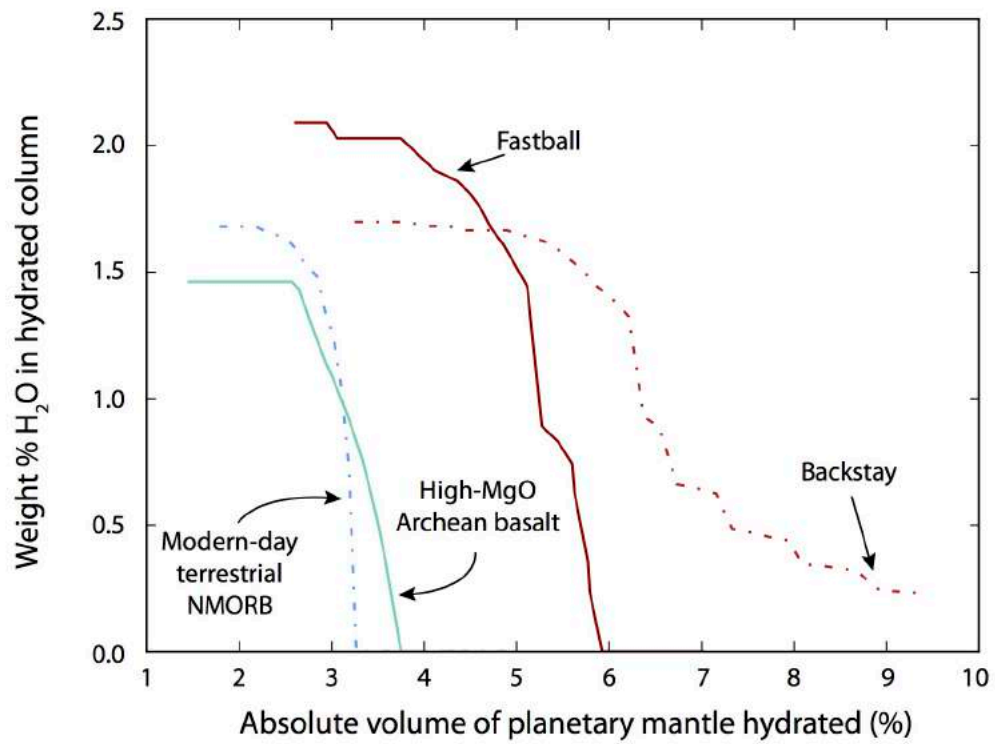


Figure 2 | Degree of mantle hydration on Earth and Mars as a function of dewatering of metamorphosed basalts.

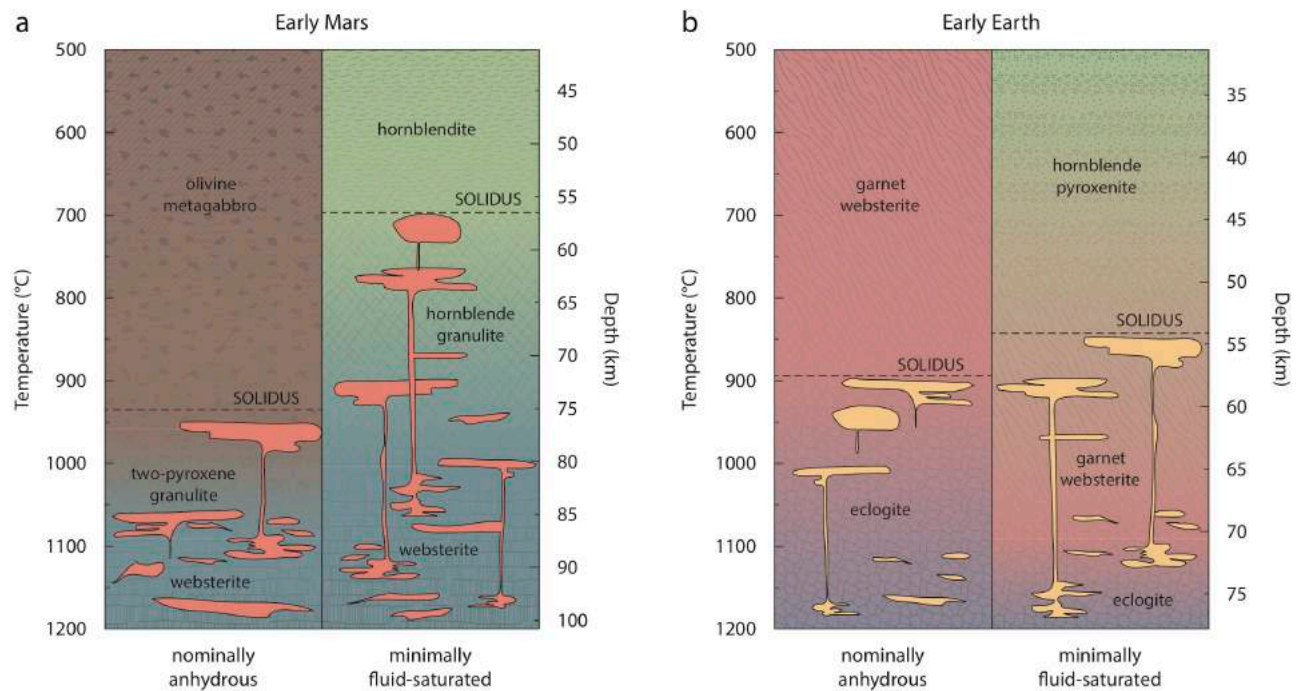


Figure 3 | Schematic cross sections through primitive (a) Martian and (b) terrestrial mafic crust. Lithological components of metamorphosed hydrated and nominally anhydrous mafic crusts on Earth and Mars based on calculated phase assemblages. Orange (Early Mars) and yellow (Early Earth) detail represent melt.

REFERENCES IN MAIN TEXT AND CAPTIONS

- 1 Peck, W. H., Valley, J. W., Wilde, S. A. & Graham, C. M. Oxygen isotope ratios and rare earth elements in 3.3 to 4.4 Ga zircons: Ion microprobe evidence for high $\delta^{18}\text{O}$ continental crust and oceans in the early Archean. *Geochimica et Cosmochimica Acta* **65**, 4215-4229, doi:10.1016/S0016-7037(01)00711-6 (2001).
- 2 Korenaga, J. Thermal evolution with a hydrating mantle and the initiation of plate tectonics in the early Earth. *Journal of Geophysical Research: Solid Earth* **116**, n/a-n/a, doi:10.1029/2011JB008410 (2011).
- 3 Lillis, R. J. *et al.* An improved crustal magnetic field map of Mars from electron reflectometry: Highland volcano magmatic history and the end of the martian dynamo. *Icarus* **194**, 575-596, doi:http://dx.doi.org/10.1016/j.icarus.2007.09.032 (2008).
- 4 Acuña, M. H. *et al.* Global Distribution of Crustal Magnetization Discovered by the Mars Global Surveyor MAG/ER Experiment. *Science* **284**, 790 (1999).
- 5 Dubinin, E. *et al.* Effects of solar irradiance on the upper ionosphere and oxygen ion escape at Mars: MAVEN observations. *Journal of Geophysical Research: Space Physics* **122**, 7142-7152, doi:10.1002/2017JA024126 (2017).
- 6 Ehlmann, B. L., Mustard, J. F. & Murchie, S. L. Geologic setting of serpentine deposits on Mars. *Geophysical Research Letters* **37**, n/a-n/a, doi:10.1029/2010gl042596 (2010).
- 7 Carter, J., Poulet, F., Bibring, J. P., Mangold, N. & Murchie, S. Hydrous minerals on Mars as seen by the CRISM and OMEGA imaging spectrometers: Updated global view.

220 *Journal of Geophysical Research: Planets* **118**, 831-858, doi:10.1029/2012je004145
 221 (2013).

222 8 Yin, A. Structural analysis of the Valles Marineris fault zone: Possible evidence for large-
 223 scale strike-slip faulting on Mars. *Lithosphere* **4**, 286-330, doi:10.1130/L192.1 (2012).

224 9 Lammer, H. *et al.* Outgassing History and Escape of the Martian Atmosphere and Water
 225 Inventory. *Space Science Reviews* **174**, 113-154, doi:10.1007/s11214-012-9943-8 (2012).

226 10 Wordsworth, R. D. in *Annual Review of Earth and Planetary Sciences* Vol. 44 381-408
 227 (2016).

228 11 Di Achille, G. & Hynek, B. M. Ancient ocean on Mars supported by global distribution of
 229 deltas and valleys. *Nature Geoscience* **3**, 459-463, doi:10.1038/ngeo891 (2010).

230 12 Carr, M. H. & Head, J. W. Martian surface/near-surface water inventory: Sources, sinks,
 231 and changes with time. *Geophysical Research Letters* **42**, 726-732,
 232 doi:10.1002/2014GL062464 (2015).

233 13 Chassefière, E., Langlais, B., Quesnel, Y. & Leblanc, F. The fate of early Mars' lost
 234 water: The role of serpentinization. *Journal of Geophysical Research E: Planets* **118**,
 235 1123-1134, doi:10.1002/jgre.20089 (2013).

236 14 Tuff, J., Wade, J. & Wood, B. J. Volcanism on Mars controlled by early oxidation of the
 237 upper mantle. *Nature* **498**, 342-345, doi:10.1038/nature12225 (2013).

238 15 Wadhwa, M. Redox state of mars' upper mantle and crust from eu anomalies in shergottite
 239 pyroxenes. *Science* **291**, 1527-1530, doi:10.1126/science.1057594 (2001).

240 16 McDonough, W. F. & Sun, S.-s. The composition of the Earth. *Chemical Geology* **120**,
 241 223-253 (1995).

242 17 Dreibus, G. & Wanke, H. Mars, A Volatile-Rich Planet. *Meteoritics* **20**, 367-381 (1985).

243 18 White, W. M. & Klein, E. M. in *Treatise on Geochemistry: Second Edition* Vol. 4 457-
 244 496 (2013).

245 19 Squyres, S. W. *et al.* Pyroclastic Activity at Home Plate in Gusev Crater, Mars. *Science*
 246 **316**, 738-742, doi:10.1126/science.1139045 (2007).

247 20 Lessel, J. & Putirka, K. New thermobarometers for martian igneous rocks, and some
 248 implications for secular cooling on Mars. *American Mineralogist* **100**, 2163-2171,
 249 doi:10.2138/am-2015-4732 (2015).

250 21 Hartel, T. H. D. & Pattison, D. R. M. Genesis of the Kapuskasing (Ontario) migmatitic
 251 mafic granulites by dehydration melting of amphibolite: The importance of quartz to
 252 reaction progress. *Journal of Metamorphic Geology* **14**, 591-611, doi:10.1046/j.1525-
 253 1314.1996.00404.x (1996).

254 22 Watson, L. L., Hutcheon, I. D., Epstein, S. & Stolper, E. M. Water on Mars - Clues from
 255 Deuterium/Hydrogen and Water Contents of Hydrous Phases in Snc Meteorites. *Science*
 256 **265**, 86-90 (1994).

257 23 Fischer, R. & Gerya, T. Early Earth plume-lid tectonics: A high-resolution 3D numerical
 258 modelling approach. *Journal of Geodynamics* **100**, 198-214,
 259 doi:10.1016/j.jog.2016.03.004 (2016).

260 24 Francois, C., Philippot, P., Rey, P. & Rubatto, D. Burial and exhumation during Archean
 261 sagduction in the East Pilbara Granite-Greenstone Terrane. *Earth and Planetary Science*
 262 *Letters* **396**, 235-251, doi:10.1016/j.epsl.2014.04.025 (2014).

263 25 Palin, R. M. & White, R. W. Emergence of blueschists on Earth linked to secular changes
 264 in oceanic crust composition. *Nature Geoscience* **9**, 60-64, doi:10.1038/ngeo2605 (2016).

265 26 Williams, Q. & Hemley, R. J. Hydrogen in the deep earth. *Annual Review Of Earth And*
 266 *Planetary Sciences* **29**, 365-418 (2001).

267 27 Gilbert, M. C. Synthesis and stability relations of the hornblende ferropargasite. *American*
 268 *Journal of Science* **264**, 698-742, doi:10.2475/ajs.264.9.698 (1966).

269 28 Carr, M. H. & Head Iii, J. W. Geologic history of Mars. *Earth and Planetary Science*
 270 *Letters* **294**, 185-203, doi:http://dx.doi.org/10.1016/j.epsl.2009.06.042 (2010).

- 29 Hauck, S. A. & Phillips, R. J. Thermal and crustal evolution of Mars. *Journal of Geophysical Research-Planets* **107**, doi:10.1029/2001je001801 (2002).
- 30 Viviano, C. E., Moersch, J. E. & McSween, H. Y. Implications for early hydrothermal environments on Mars through the spectral evidence for carbonation and chloritization reactions in the Nili Fossae region. *Journal of Geophysical Research: Planets* **118**, 1858-1872, doi:10.1002/jgre.20141 (2013).
- 31 Poli, S. & Schmidt, M. W. Petrology of subducted slabs. *Annual Review Of Earth And Planetary Sciences* **30**, 207-235 (2002).
- 32 Mouginot, J., Pommerol, A., Beck, P., Kofman, W. & Clifford, S. M. Dielectric map of the Martian northern hemisphere and the nature of plain filling materials. *Geophysical Research Letters* **39**, n/a-n/a, doi:10.1029/2011gl050286 (2012).
- 33 Usui, T., Alexander, C. M. O. D., Wang, J., Simon, J. I. & Jones, J. H. Meteoritic evidence for a previously unrecognized hydrogen reservoir on Mars. *Earth and Planetary Science Letters* **410**, 140-151, doi:10.1016/j.epsl.2014.11.022 (2015).

METHODS

Petrological modelling procedures

All phase diagrams were constructed using THERMOCALC v. 3.45i³⁴ and the internally consistent thermodynamic data set ds62 (ref. ³⁵; updated 6/2/2012). Modelling was performed in the Na₂O–CaO–K₂O–FeO–MgO–Al₂O₃–SiO₂–H₂O–TiO₂–O₂ (NCKFMASHTO) compositional system using the following activity–composition relations for solid-solution phases: tonalitic melt, clinoamphibole, and augitic clinopyroxene³⁶, orthopyroxene, garnet, biotite, muscovite, chlorite, and ilmenite–hematite³⁷, plagioclase and K-feldspar³⁸, olivine and epidote³⁵, and spinel–magnetite³⁹. Pure phases included albite, rutile, sphene, quartz, and H₂O. The initial bulk-rock compositions used for modelling of all protoliths were converted from wt. % oxides, as reported in each original study (Table 1, Extended Data), to mol. % oxides, with fluid contents adjusted on an individual basis, as described below. The software and data files used to generate the phase diagrams may be downloaded from <http://www.metamorph.geo.uni-mainz.de/thermocalc>

For modelling under water-present conditions (Table 2, Extended Data), bulk-rock fluid contents were individually fixed such that each lithology was minimally saturated at the intersection of the relevant geotherm/aerothrm and its solidus. Here, we define minimal saturation as the equilibrium phase assemblage containing 0.5 mol. % of free water (H₂O) at the point of first melting. Additional H₂O was present within the bulk-rock composition in each case as structurally bound water within hydrous minerals. For nominally anhydrous conditions, the absolute amount of H₂O within each bulk-rock composition was fixed at a total of 0.5 mol. % (prior to melt loss), with these bulk compositions shown in (Table 3, Extended Data). Invariably, free H₂O was absent from calculated assemblages, with all bulk-rock H₂O at the solidus being structurally bound within hydrous phases. For internal consistency and ease of comparison, calculations for all rock types used a molar bulk-rock $X_{Fe^{3+}}$ [= Fe₂O₃/(Fe₂O₃+FeO)] value of 0.1 (cf. refs. ^{40,41}). Uncertainty on the absolute positions of assemblage field boundaries in *P–T* space generally do not exceed ±1 kbar and ±50 °C for low variance equilibria at the 2σ level^{42,43}. Such variation is largely a function of propagated uncertainty on end-member thermodynamic properties within the internally consistent dataset. However, as all phase diagrams were calculated using the same dataset and *a–x* relations, similar absolute errors associated with dataset end-members cancel, and calculated phase equilibria are expected to be relatively accurate to within ±0.2 kbar and ±10–15 °C^{42,43}.

The petrological effects of open-system melting and melt loss were modelled using manipulation of the read-bulk-info (RBI) matrix⁴⁴. We assumed that melt loss was a cyclical process, with drainage events occurring each time a rock's melt proportion reaches a rheologically critical threshold. The melt-extraction threshold for intermediate and felsic magmas is around 20–30%^{45,46}, and we used the upper limit of this range (30%) as our transition point. Ten-percent of this melt was assumed to remain in the source rock following each drainage event, given that a minimum proportion of ~8% melt must be present in a rock in order to overcome the liquid percolation threshold⁴⁵. From a computational standpoint, this was implemented by reducing the calculated modal proportion of the melt phase in the RBI matrix from 0.3 to 0.1 at each relevant *P–T* point along the relevant geotherm/aerothrm.

Petrological modelling: theory and application

The petrological modelling employed herein relies upon a thermodynamic-equilibrium model of metamorphism, in which it is assumed that equilibrium on a local scale is maintained among mineral, fluid, and melt phases during the evolution of the rock⁴⁷⁻⁵⁰. A model is used to represent the thermodynamics of each phase, comprising properties for its end-members combined with activity–composition (a – x) relations to describe their mixing in solid solution⁵¹. This allows calculation of the equilibrium compositions and proportions of phases (mineral, melt, and aqueous fluid) in the stable assemblage, at given pressure, temperature and bulk composition⁵². Equilibrium conditions in such a system require the equality of chemical potentials of each component in all phases, and must conform to the constraints of mass balance. Such calculations are frequently performed in metamorphic geology, with the help of appropriate software^{34,52}, to construct pseudosections: phase diagrams that map out the thermodynamically stable assemblages that would form in a particular bulk-rock composition across P – T space^{50,53}. This calculation procedure and the a – x relations utilised are mature, and have been demonstrably effective in both forward (predictive) and inverse (descriptive) petrological modelling studies (cf. refs. ⁵³⁻⁵⁵ for representative examples). All phase abbreviations are after ⁵⁶, alongside “L” or “Melt” for silicate melt.

Calculated bulk-rock density profiles

Calculated bulk-rock densities considered all phases in the equilibrium assemblage (solids, aqueous fluids, and melt) at each P – T point. Metamorphism of terrestrial NMORB in a hydrous system produces a relatively low density metamorphic product, owing to the abundance of H₂O leading to the formation of amphibole and biotite (Extended Data - Fig. 5). In contrast, relatively dense garnet and pyroxene form in the nominally anhydrous case (Extended Data - Fig. 6). We considered an open-system scenario in this work, whereby melt generated during metamorphism can reach a critical escape threshold and leave the local environment, which is a realistic approximation of a natural system. Differential degrees of melt-loss lead to a density inversion between terrestrial and Martian metabasalts at upper amphibolite-/granulite-facies conditions. As shown by our calculations, partial melting begins earlier (i.e. at lower temperature) in a hydrated NMORB than in a nominally anhydrous equivalent, owing to the abundance of amphibole in the former. In addition, melt generation is more voluminous, and quartz and feldspar are preferentially consumed as part of the melt-producing reactions. The density inversion for hydrous versus nominally anhydrous NMORB occurs at the point of first melt extraction, when the former becomes melt-depleted, and the residual phase assemblage is entirely anhydrous (Grt+Aug). As bulk-rock density was calculated for the entire petrological system (i.e. solid plus melt, prior to extraction), melt loss from the initially hydrated protolith causes the remaining solid residue to become denser than the initially nominally anhydrous equivalent, which has not yet accumulated sufficient melt to cause a drainage event. Density differences between both studied Martian basalts are also a result of bulk-rock composition and melt fertility, with the relatively high alkali content of the Fastball protolith producing low-density feldspars in anhydrous conditions, but relatively dense amphibole in a water-rich environment.

376 Thermal modelling procedures

377 The thermal model was constructed analytically as a solution to the one dimensional heat flow
 378 problem in a plate⁶¹, including an additional source term to account for radiogenic heat
 379 production^{62,63}

$$\frac{\partial T(x, t)}{\partial t} = \kappa \frac{\partial^2 T(x, t)}{\partial x^2} + A_0 \exp\left(-\frac{t - t_0}{\tau_r}\right)$$

380 where κ is the thermal diffusivity, t_0 is today, and A_0 is the present-day radiogenic heat
 381 production rate with time constant τ_r ⁶³. We apply boundary conditions
 382

$$T(x = 0, t) = 0$$

$$T(x = L, t) = T_p \exp\left(-\frac{t - t_0}{\tau_s}\right)$$

383 where T_p is the mantle potential temperature, τ_s is the secular cooling time constant, and L is the
 384 lithospheric thickness. Initial conditions at the time of lithospheric generation take into account
 385 the secular cooling
 386

$$T(x, t = 0) = T_p \exp\left(-\frac{t - t_0}{\tau_s}\right)$$

387 with the same parameters as the boundary conditions above. The solution may be expressed as a
 388 Fourier Series:
 389

$$\begin{aligned} T(x, t) = & T_p e^{-\frac{t-t_0}{\tau_s}} \left(\frac{x}{L}\right) + 2 \sum_{n=1}^{\infty} \sin\left(\frac{\pi n x}{L}\right) \left[\frac{A_0 ((-1)^n - 1) \tau_r \left(e^{-\frac{t-t_0}{\tau_r}} - e^{-n^2 \pi^2 \kappa t}\right)}{(\pi n - \pi^3 \kappa n^3 \tau_r)} \right. \\ & \left. + \frac{T_p e^{-n^2 \pi^2 \kappa t}}{\pi n} + \frac{T_p \kappa (-1)^n \left(e^{-\frac{t-t_0}{\tau_s}} - e^{-n^2 \pi^2 \kappa t}\right)}{\pi n - \pi^3 \kappa n^3 \tau_s} \right] \end{aligned} \quad (1)$$

390 which we evaluate the first 200 terms to produce each geotherm and aerotherm.
 391
 392

393 To explore the uncertainty on the radiogenic heat production and secular cooling rates, we
 394 sampled 3240 geotherms and 3780 aerotherms, with a range of cooling rates on Earth of $20\text{Ga} <$
 395 $\tau_s < 45\text{Ga}$ and Mars of $10\text{Ga} < \tau_s < 40\text{Ga}$, and radiogenic heat production rates of $0.1 \mu\text{Wm}^{-3} < A_0$
 396 $< 1.0 \mu\text{Wm}^{-3}$. This resulted in a range of mantle potential temperatures for early Earth $1500^\circ\text{C} <$
 397 $T_p < 1600^\circ\text{C}$, late Earth $1300^\circ\text{C} < T_p < 1400^\circ\text{C}$, early Mars $1600^\circ\text{C} < T_p < 1700^\circ\text{C}$ ^{64,65}, and late
 398 Mars $1350^\circ\text{C} < T_p < 1450^\circ\text{C}$ ⁶⁶. We then took the mean and 99% confidence interval of 150Ma
 399 lithosphere for each family of thermal models, equivalent to a T_p of $1550/1650^\circ\text{C}$ and
 400 $1350/1400^\circ\text{C}$ for the primitive and evolved rocks of Earth/Mars respectively, as the input for the
 401 petrological modelling and error estimates.
 402

403 To assess the validity of a 1D model when used as an approximation for a spherical shell we
 404 compared the steady state ($\tau_s \rightarrow \infty$, $t \rightarrow \infty$) solution of eqn (1) to the steady state spherical shell
 405 solution,

$$T(r) = \frac{(R - L)(R - r)}{Lr} T_m \quad (2)$$

406

where R is the planetary radius, L the lithospheric thickness, and r the radial position. We found that the error obtained using a 1D approach compared to a spherical shell is 0.9% for the Earth and 1.77% for Mars, which is well within the uncertainty on the other parameters defined above.

Numerical simulations for the temperature structure were also calculated a posteriori from the results of the petrological modelling to account for depth dependent variations in the thermal diffusivity (κ) due to density variations in the bulk mineral assemblages. We found that the maximum deviation in the thermal structure due to compositional effects to be <1.5% for times after 10 Ma and thus could also be safely neglected, in agreement with other recent work⁶⁷.

Data Availability Statement: Authors can confirm that all relevant data are included in the paper and/ or its supplementary information files

REFERENCES.

- 34 Powell, R. & Holland, T. J. B. An internally consistent dataset with uncertainties and correlations: 3. Applications to geobarometry, worked examples and a computer program. *Journal of Metamorphic Geology* **6**, 173-204, doi:10.1111/j.1525-1314.1988.tb00415.x (1988).
- 35 Holland, T. J. B. & Powell, R. An improved and extended internally consistent thermodynamic dataset for phases of petrological interest, involving a new equation of state for solids. *Journal of Metamorphic Geology* **29**, 333-383, doi:10.1111/j.1525-1314.2010.00923.x (2011).
- 36 Green, E. C. R. *et al.* Activity-composition relations for the calculation of partial melting equilibria in metabasic rocks. *Journal of Metamorphic Geology* **34**, 845-869, doi:10.1111/jmg.12211 (2016).
- 37 White, R. W., Powell, R., Holland, T. J. B., Johnson, T. E. & Green, E. C. R. New mineral activity-composition relations for thermodynamic calculations in metapelitic systems. *Journal of Metamorphic Geology* **32**, 261-286, doi:10.1111/jmg.12071 (2014).
- 38 Holland, T. & Powell, R. Activity-composition relations for phases in petrological calculations: an asymmetric multicomponent formulation. *Contributions to Mineralogy and Petrology* **145**, 492-501, doi:10.1007/s00410-003-0464-z (2003).
- 39 White, R. W., Powell, R. & Clarke, G. L. The interpretation of reaction textures in Fe-rich metapelitic granulites of the Musgrave Block, central Australia: constraints from mineral equilibria calculations in the system K₂O-FeO-MgO-Al₂O₃-SiO₂-H₂O-TiO₂-Fe₂O₃. *Journal of Metamorphic Geology* **20**, 41-55, doi:10.1046/j.0263-4929.2001.00349.x (2002).
- 40 Berry, A. J., Danyushevsky, L. V., O'Neill, H. S. C., Newville, M. & Sutton, S. R. Oxidation state of iron in komatiitic melt inclusions indicates hot Archaean mantle. *Nature* **455**, 960-U942, doi:10.1038/nature07377 (2008).
- 41 Christie, D. M., Carmichael, I. S. E. & Langmuir, C. H. Oxidation-States of Mid-ocean Ridge Basalt Glasses. *Earth and Planetary Science Letters* **79**, 397-411 (1986).

454 42 Powell, R. & Holland, T. J. B. On thermobarometry. *Journal of Metamorphic Geology* **26**,
455 155-179, doi:10.1111/j.1525-1314.2007.00756.x (2008).

456 43 Palin, R. M., Weller, O. M., Waters, D. J. & Dyck, B. Quantifying geological uncertainty
457 in metamorphic phase equilibria modelling; a Monte Carlo assessment and implications
458 for tectonic interpretations. *Geoscience Frontiers* **7**, 591-607,
459 doi:10.1016/j.gsf.2015.08.005 (2016).

460 44 White, R. W. *Tutorial for using the readbulkinf (rbi) script.*,
461 <<http://www.metamorph.geo.uni-mainz.de/thermocalc/tutorials/-rbi>> (2010).

462 45 Vigneresse, J. L., Barbey, P. & Cuney, M. Rheological transitions during partial melting
463 and crystallization with application to felsic magma segregation and transfer. *Journal of*
464 *Petrology* **37**, 1579-1600, doi:10.1093/petrology/37.6.1579 (1996).

465 46 Rosenberg, C. L. & Handy, M. R. Experimental deformation of partially melted granite
466 revisited: implications for the continental crust. *Journal of Metamorphic Geology* **23**, 19-
467 28, doi:10.1111/j.1525-1314.2005.00555.x (2005).

468 47 Khorzhinskii, D. S. *Physicochemical Basis of the Analysis of the Paragenesis of Minerals*.
469 Consultants Bureau, (1959).

470 48 Thompson, J. B. Local equilibrium in metasomatic processes. *Researches in geochemistry*
471 **1**, 427-457 (1959).

472 49 Guiraud, M., Powell, R. & Rebay, G. H₂O in metamorphism and unexpected behaviour in
473 the preservation of metamorphic mineral assemblages. *Journal of Metamorphic Geology*
474 **19**, 445-454, doi:10.1046/j.0263-4929.2001.00320.x (2001).

475 50 Powell, R., Holland, T. & Worley, B. Calculating phase diagrams involving solid
476 solutions via non-linear equations, with examples using THERMOCALC. *Journal of*
477 *Metamorphic Geology* **16**, 577-588, doi:10.1111/j.1525-1314.1998.00157.x (1998).

478 51 Connolly, J. A. D. Multivariable phase diagrams – an algorithm based on generalized
479 thermodynamics. *American Journal of Science* **290**, 666-718 (1990).

480 52 Connolly, J. A. D. Computation of phase equilibria by linear programming: A tool for
481 geodynamic modeling and its application to subduction zone decarbonation. *Earth and*
482 *Planetary Science Letters* **236**, 524-541, doi:10.1016/j.epsl.2005.04.033 (2005).

483 53 Palin, R. M. *et al.* High-grade metamorphism and partial melting of basic and
484 intermediate rocks. *Journal of Metamorphic Geology* **34**, 871-892,
485 doi:10.1111/jmg.12212 (2016).

486 54 Carson, C. J., Powell, R. & Clarke, G. L. Calculated mineral equilibria for eclogites in
487 CaO-Na₂O-FeO-MgO-Al₂O₃-SiO₂-H₂O: application to the Pouébo Terrane, Pam
488 Peninsula, New Caledonia. *Journal of Metamorphic Geology* **17**, 9-24 (1999).

489 55 White, R. W., Powell, R., Holland, T. J. B. & Worley, B. A. The effect of TiO₂ and
490 Fe₂O₃ on metapelitic assemblages at greenschist and amphibolite facies conditions:
491 mineral equilibria calculations in the system K₂O-FeO-MgO-Al₂O₃-SiO₂-H₂O-TiO₂-
492 Fe₂O₃. *Journal of Metamorphic Geology* **18**, 497-511 (2000).

493 56 Kretz, R. Symbols of rock-forming minerals. *American Mineralogist* **68**, 277-279 (1983).

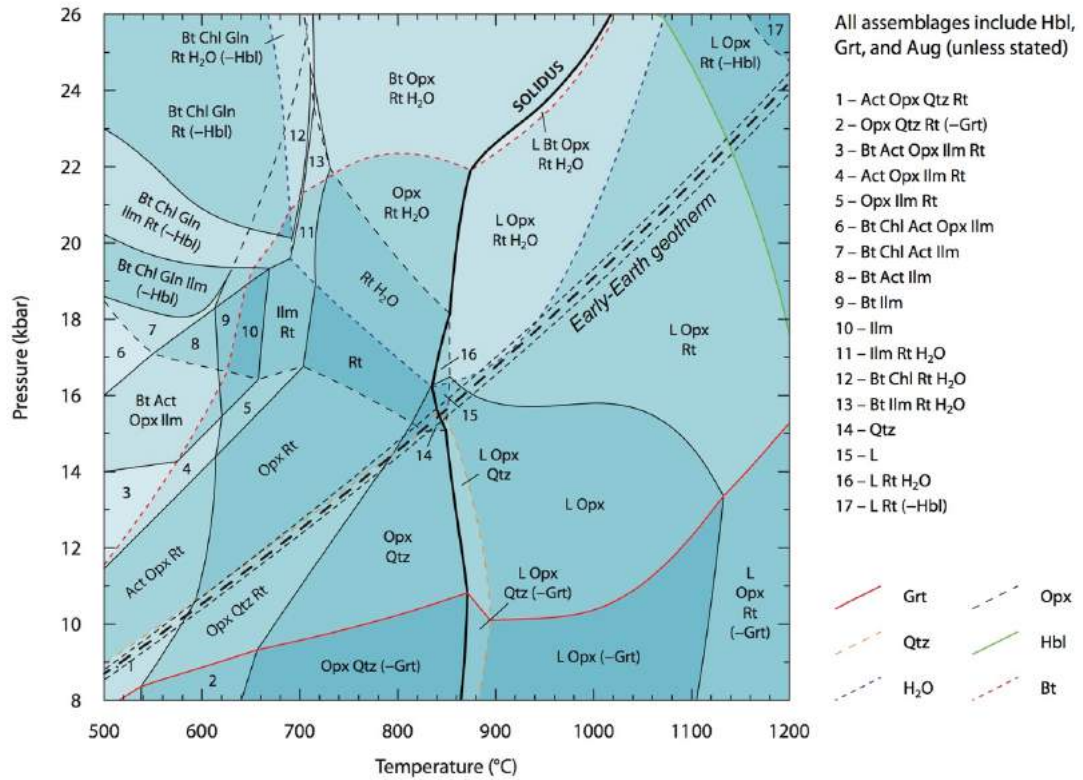
494 57 Kato, Y. & Nakamura, K. Origin and global tectonic significance of Early Archean cherts
495 from the Marble Bar greenstone belt, Pilbara Craton, Western Australia. *Precambrian*
496 *Research* **125**, 191-243, doi:10.1016/s0301-9268(03)00043-3 (2003).

497 58 Gale, A., Dalton, C. A., Langmuir, C. H., Su, Y. J. & Schilling, J. G. The mean
498 composition of ocean ridge basalts. *Geochemistry Geophysics Geosystems* **14**, 489-518,
499 doi:10.1029/2012gc004334 (2013).

500 59 Squyres, S. W. *et al.* Pyroclastic Activity at Home Plate in Gusev Crater, Mars. *Science*
501 **316**, 738-742, doi:10.1126/science.1139045 (2007).

502 60 McSween, H. Y. *et al.* Alkaline volcanic rocks from the Columbia Hills, Gusev Crater,
503 Mars. *Journal Of Geophysical Research-Planets* **111**, -, doi:Artn E09s91
504 Doi 10.1029/2006je002698 (2006).

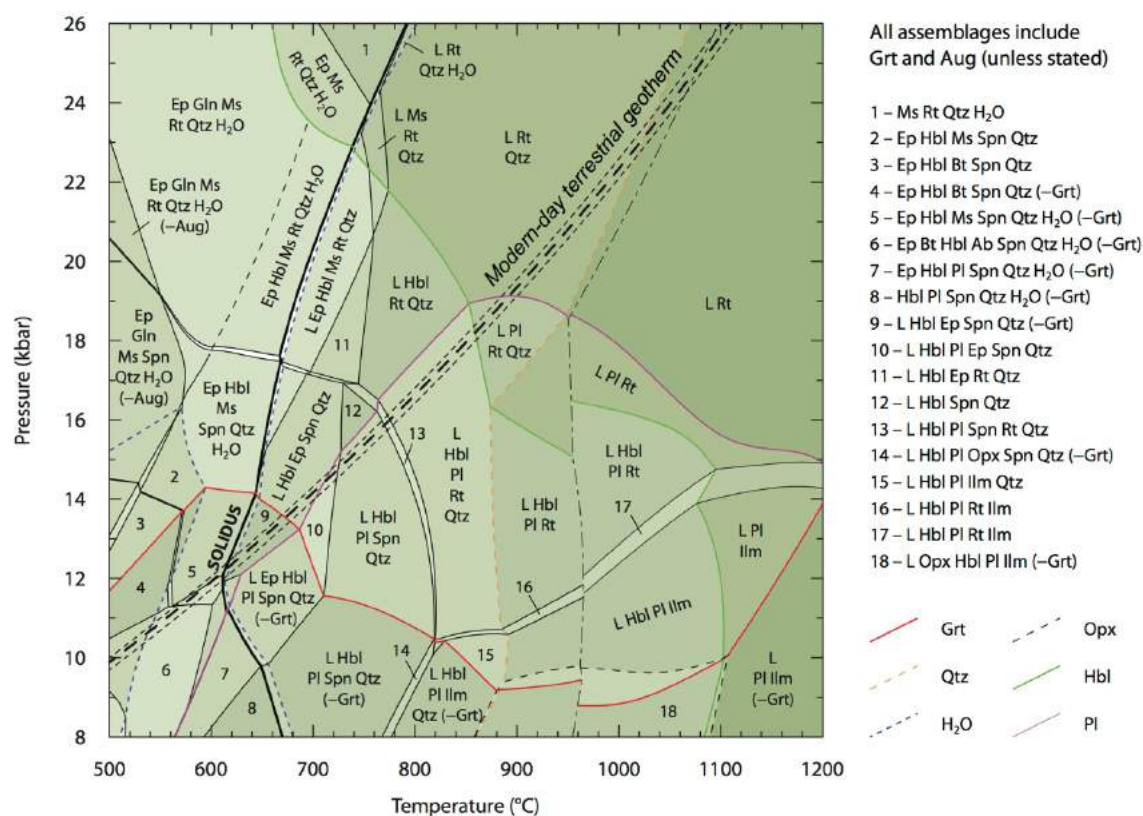
- 61 Parsons, B. & Sclater, J. G. An analysis of the variation of ocean floor bathymetry and
62 heat flow with age. *Journal of Geophysical Research* **82**, 803-827,
63 doi:10.1029/JB082i005p00803 (1977).
- 64 Driscoll, P. & Bercovici, D. On the thermal and magnetic histories of Earth and Venus:
65 Influences of melting, radioactivity, and conductivity. *Physics of the Earth and Planetary
66 Interiors* **236**, 36-51, doi:10.1016/j.pepi.2014.08.004 (2014).
- 67 Michaut, C. & Jaupart, C. Secular cooling and thermal structure of continental
lithosphere. *Earth and Planetary Science Letters* **257**, 83-96,
doi:10.1016/j.epsl.2007.02.019 (2007).
- Herzberg, C., Condie, K. & Korenaga, J. Thermal history of the Earth and its petrological
expression. *Earth and Planetary Science Letters* **292**, 79-88,
doi:10.1016/j.epsl.2010.01.022 (2010).
- Lessel, J. & Putirka, K. New thermobarometers for martian igneous rocks, and some
implications for secular cooling on Mars. *American Mineralogist* **100**, 2163-2171,
doi:10.2138/am-2015-4732 (2015).
- Filiberto, J. & Dasgupta, R. Constraints on the depth and thermal vigor of melting in the
Martian mantle. *Journal of Geophysical Research: Planets* **120**, 109-122,
doi:10.1002/2014je004745 (2015).
- McKenzie, D., Jackson, J. & Priestley, K. Thermal structure of oceanic and continental
lithosphere. *Earth and Planetary Science Letters* **233**, 337-349,
doi:10.1016/j.epsl.2005.02.005 (2005).



[Extended Data – fig 1]

[Extended Data – fig 1 **Title**] Palaeoarchean high-Mg basalt Pressure–temperature (P – T) pseudosection

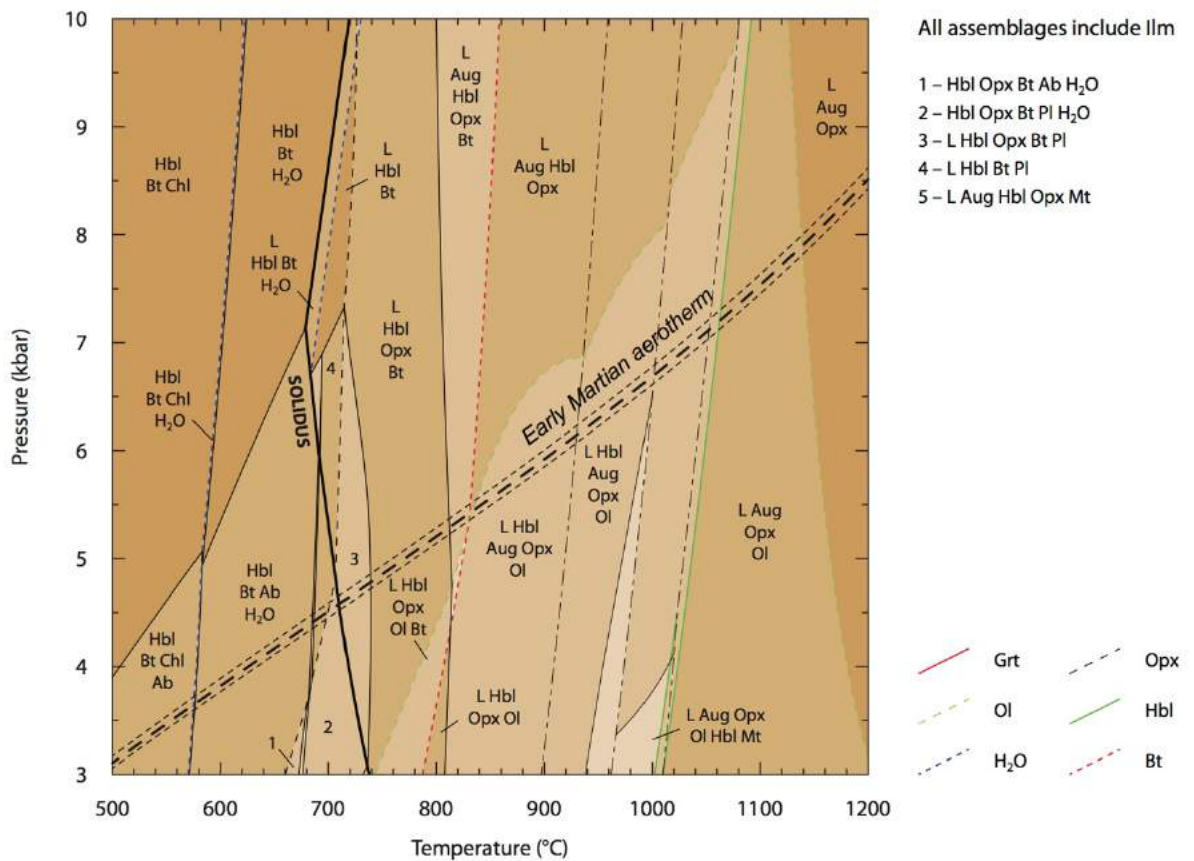
[Extended Data – **fig 1 legend**] Pressure–temperature (P – T) pseudosection calculated for the bulk-rock composition of Palaeoarchean high-Mg basalt sample 02MB256 from ⁵⁷. Some small fields are unlabelled for clarity. Bold dashed line labelled ‘*Early-Earth geotherm*’ represents the P – T profile calculated via thermal modelling, and is enveloped by short-dashed lines representing upper and lower confidence intervals on these values.



[Extended Data – fig 2]

[Extended Data – fig 2 Title] NMORB Pressure–temperature (P – T) pseudosection

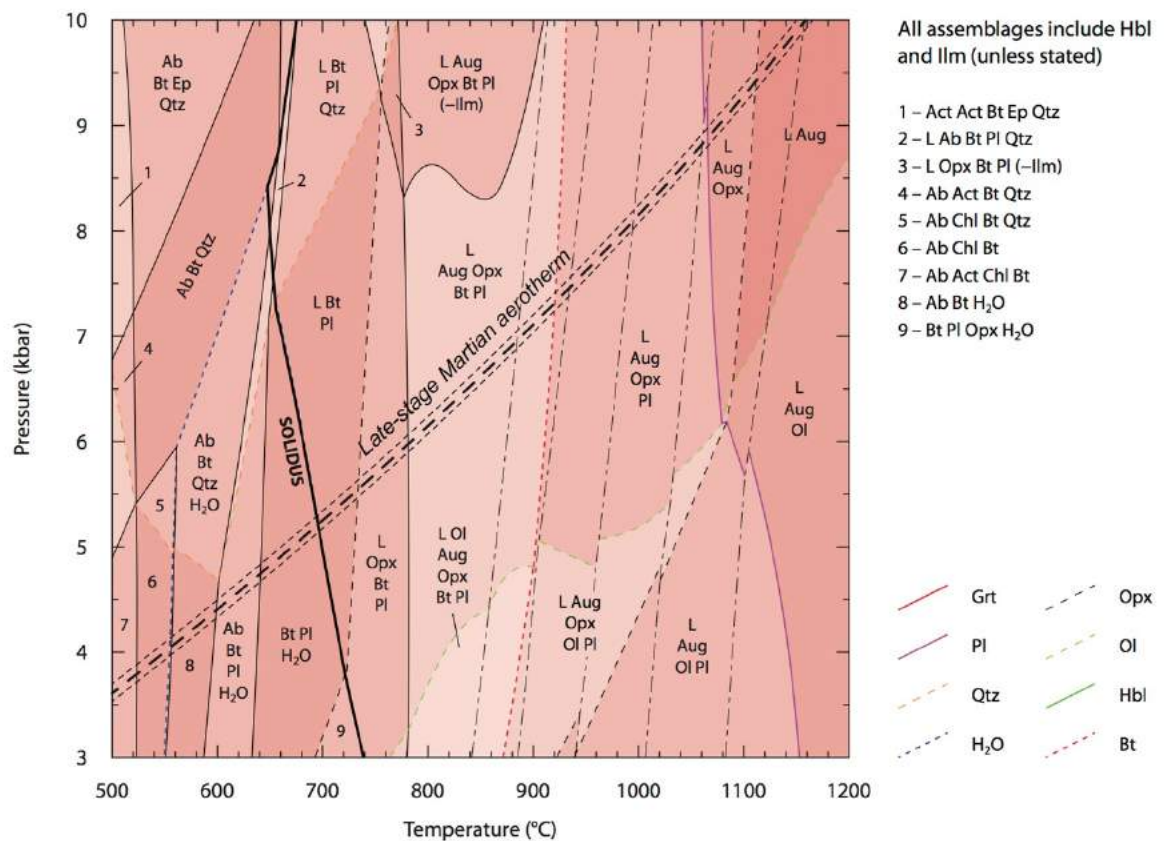
[Extended Data – fig 2 legend] Pressure–temperature (P – T) pseudosection calculated for the bulk-rock composition of NMORB from ⁵⁸. Some small fields are unlabelled for clarity. Bold dashed line labelled ‘*Modern-day terrestrial geotherm*’ represents the P – T profile calculated via thermal modelling, and is enveloped by short-dashed lines representing upper and lower confidence intervals on these values.



[Extended Data – fig 3]

[Extended Data – fig 3 **Title**] Fastball (Mars) Pressure–temperature (P – T) pseudosection

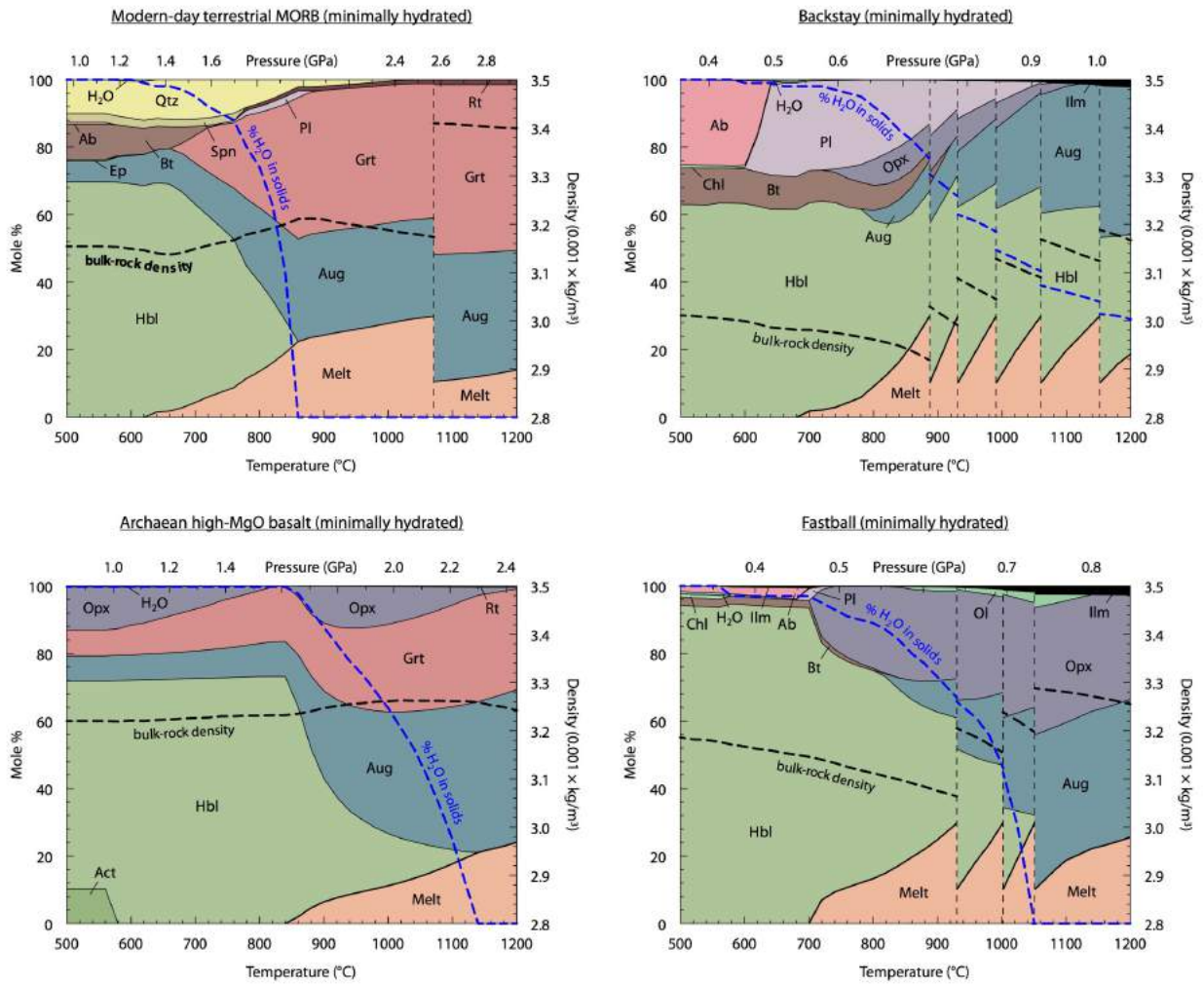
[Extended Data – **fig 3 legend**] Pressure–temperature (P – T) pseudosection calculated for the bulk-rock composition of Fastball from⁵⁹. Some small fields are unlabelled for clarity. Bold dashed line labelled ‘*Early Martian aerotherm*’ represents the P – T profile calculated via thermal modelling, and is enveloped by short-dashed lines representing upper and lower confidence intervals on these values.



[Extended Data – fig 4]

[Extended Data – fig 4 **Title**] Backstay (Mars) Pressure–temperature (P – T) pseudosection

[Extended Data – **fig 4 legend**] Pressure–temperature (P – T) pseudosection calculated for the bulk-rock composition of Backstay from ⁶⁰. Some small fields are unlabelled for clarity. Bold dashed line labelled ‘*Late-stage Martian aerotherm*’ represents the P – T profile calculated via thermal modelling, and is enveloped by short-dashed lines representing upper and lower confidence intervals on these values.

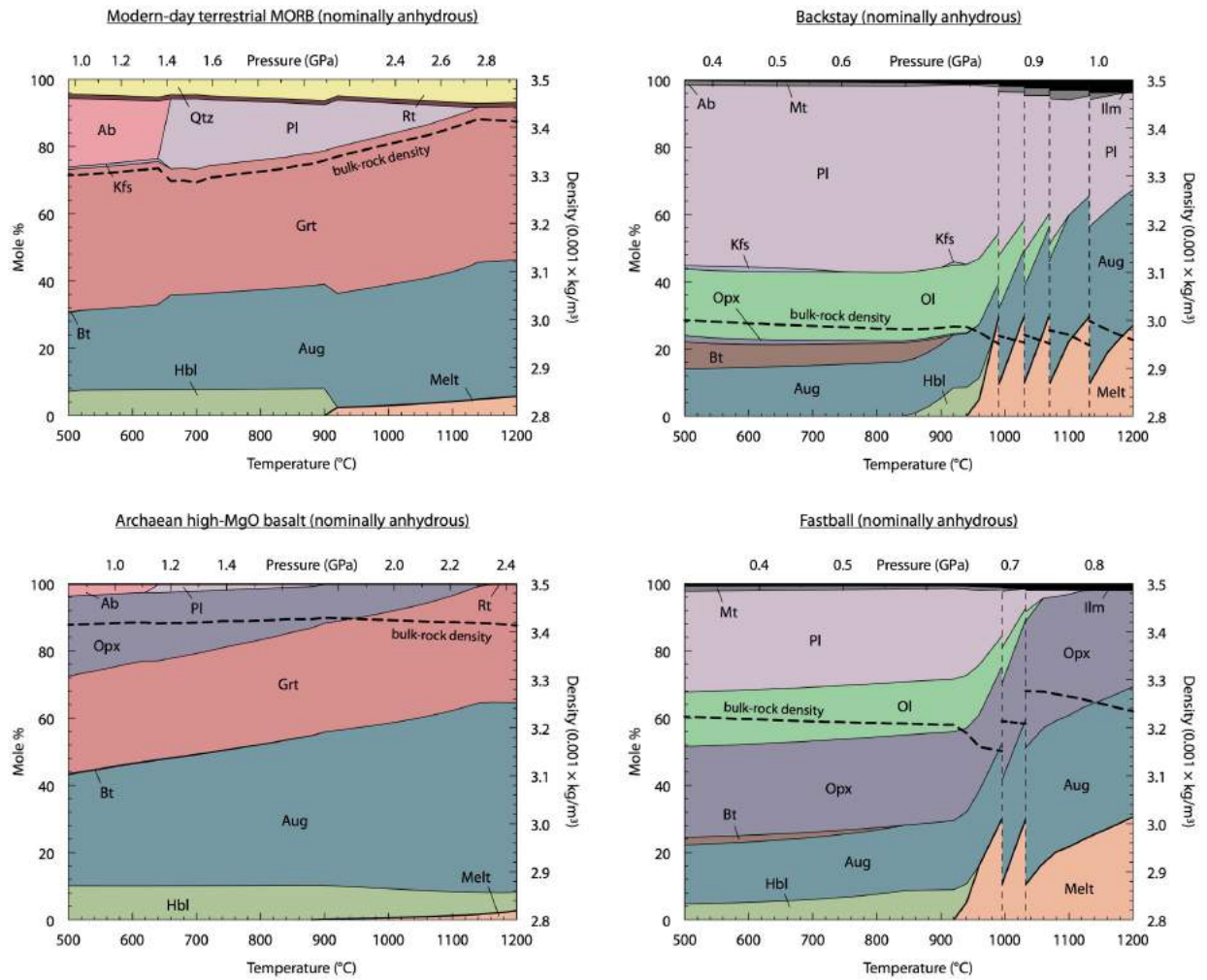


[Extended Data – fig 5]

[Extended Data – fig 5 Title] Hydrated terrestrial and Martian basalts mineral proportions

[Extended Data – fig 5 legend] Calculated mineral proportions, bulk-rock densities, and water contents during metamorphism of hydrated terrestrial and Martian basalts along their respective planetary geotherms and aerotherms.

Vertical dashed lines represent pressure-temperature (P - T) points at which melt extraction events occurred (see *Methods*).



[Extended Data – fig 6]

[Extended Data – fig 6 Title] Nominally anhydrous terrestrial and Martian basalts mineral proportions

[Extended Data – fig 6 legend] Calculated mineral proportion and bulk-rock densities during metamorphism of nominally anhydrous terrestrial and Martian basalts along their respective planetary geotherms and aerotherms.

Vertical dashed lines represent pressure-temperature (P - T) points at which melt extraction events occurred (see *Methods*).

Table 1

Lithology	SiO ₂	TiO ₂	Al ₂ O ₃	Fe ₂ O ₃	FeO	MgO	CaO	Na ₂ O	K ₂ O
High-Mg basalt ⁵⁷	48.75	0.48	10.32	N.R.	10.89	16.19	10.49	1.42	0.03
N-MORB ⁵⁸	50.42	1.53	15.13	N.R.	9.81	7.76	11.35	2.83	0.14
Fastball ⁵⁹	45.30	0.67	7.85	9.26	8.54	12.0	5.80	2.35	0.23
Backstay ⁶⁰	49.60	0.93	13.30	3.33	10.70	8.32	6.05	4.16	1.07

[Extended – Data table 1 – Title] Bulk compositions of mafic crustal components used in this work (weight % oxides).

[Legend]: - N.R. = not reported. ⁵⁷Kato and Nakamura (2003), sample 02MB256; ⁵⁸Gale et al. (2013); ⁵⁹Squyres *et al.* (2007); ⁶⁰McSween *et al.* (2006), Backstay “preferred composition”.

Table 2

Lithology	Stage	H ₂ O	SiO ₂	Al ₂ O ₃	CaO	MgO	FeO ^{tot}	K ₂ O	Na ₂ O	TiO ₂	O
High-Mg basalt	0	4.59	45.82	5.72	10.56	22.68	8.56	0.02	1.29	0.34	0.43
N-MORB	0	5.58	49.77	8.80	12.00	11.42	8.10	0.09	2.71	1.14	0.40
	1	2.27	47.52	8.71	14.13	13.86	9.74	0.04	1.86	1.39	0.49
Fastball	0	6.63	45.68	4.67	6.27	18.04	15.02	0.15	2.30	0.51	0.75
	1	4.21	45.15	4.26	7.31	20.52	15.23	0.09	1.69	0.63	0.92
	2	2.57	44.97	3.82	8.41	22.71	14.41	0.05	1.17	0.77	1.13
	3	1.21	44.86	3.21	9.57	24.80	13.38	0.02	0.63	0.95	1.39
Backstay	0	5.66	49.91	7.89	6.52	12.48	11.53	0.69	4.06	0.70	0.58
	1	4.39	48.24	7.83	7.76	14.27	11.81	0.56	3.56	0.87	0.71
	2	3.74	46.35	7.79	9.19	16.01	11.51	0.35	3.11	1.07	0.88
	3	3.36	44.41	7.75	10.79	17.65	10.80	0.22	2.62	1.33	1.08
	4	3.05	42.53	7.61	12.50	19.16	9.90	0.13	2.14	1.64	1.34
	5	2.65	41.17	7.50	14.33	20.04	8.75	0.09	1.79	2.03	1.66

[Extended – Data table 2 – Title] Bulk compositions used in phase equilibrium modelling (molar % oxides) under minimally fluid-saturated conditions.

[Legend]: - *N.B.* O contents were calculated assuming a bulk-rock $X\text{Fe}^{3+} = \text{Fe}_2\text{O}_3/(\text{FeO}+\text{Fe}_2\text{O}_3) = 0.1$, where $X\text{Fe}^{3+} = (2 \times \text{O})/\text{FeO}^{\text{tot}}$. Stage numbers refer to the number of melt-extraction events, and the associated bulk compositions for numbers ≥ 1 represent increasingly melt-depleted residua (i.e. 0 = initial undepleted bulk composition; 1 = residual bulk composition following one melt-loss event, 2 = residual bulk composition following two melt-loss events etc.)

Table 3.

Lithology	Stage	H ₂ O	SiO ₂	Al ₂ O ₃	CaO	MgO	FeO ^{tot}	K ₂ O	Na ₂ O	TiO ₂	O
High-Mg basalt	0	0.50	47.78	5.96	11.02	23.65	8.93	0.02	1.35	0.35	0.45
N-MORB	0	0.50	52.45	9.28	12.65	12.03	8.53	0.09	2.85	1.20	0.42
Fastball	0	0.50	48.68	4.97	6.68	19.22	16.00	0.16	2.45	0.54	0.80
	1	0.21	47.81	4.53	7.83	20.92	15.13	0.09	1.84	0.67	0.98
	2	0.09	46.92	4.00	9.18	22.63	13.97	0.04	1.14	0.83	1.21
Backstay	0	0.50	52.64	8.32	6.88	13.16	12.16	0.72	4.28	0.74	0.61
	1	0.21	52.38	8.60	8.13	13.54	10.69	0.62	4.16	0.93	0.76
	2	0.09	52.03	8.94	9.67	13.57	9.09	0.52	3.98	1.16	0.95
	3	0.04	51.37	9.30	11.54	13.25	7.75	0.43	3.69	1.45	1.19
	4	0.02	50.25	9.61	13.77	12.62	6.87	0.32	3.25	1.81	1.48

[Extended Data – Data table 3 – Title] Bulk compositions used in phase equilibrium modelling (molar % oxides) under nominally dry conditions.

[Legend]: *N.B.* O contents were calculated assuming a bulk-rock $X\text{Fe}^{3+} = \text{Fe}_2\text{O}_3/(\text{FeO}+\text{Fe}_2\text{O}_3) = 0.1$, where $X\text{Fe}^{3+} = (2 \times \text{O})/\text{FeO}^{\text{tot}}$. Stage number nomenclature is the same as for Extended Data Table 2.